© 2011 Hongxiang Tian

VOLUMETRIC HEAT CAPACITY ENHANCEMENT IN ULTRATHIN FLUOROCARBON POLYMERS FOR CAPACITIVE THERMAL MANAGEMENT

BY

HONGXIANG TIAN

THESIS

Submitted in partial fulfillment of the requirements
for the degree of Master of Science in Mechanical Engineering
in the Graduate College of the
University of Illinois at Urbana-Champaign, 2011

Urbana, Illinois

Adviser:

Assistant Professor Sanjiv Sinha

ABSTRACT

Capacitive thermal management in electronics requires an enhancement in the volumetric storage density of compatible materials to approximately 1 GJ/m^3. We investigate potential enhancement in sensible storage density arising from size effects in thin polymer films. We design and fabricate a micro-calorimeter to measure the volumetric heat capacity of nanometer scale thin fluorocarbon polymer films. The storage density increases approximately three times as the film thickness decreases from 27 nm to 12 nm. Using the Debye theory of phonons, we relate this behavior to an increase in the Grüneisen parameter with decreasing film thickness. This work advances the understanding of size dependence in the heat capacity of amorphous polymers as well as highlights their potential for capacitive thermal management.

To my parents and sister, for their love and support.

ACKNOWLEDGMENTS

I would like to thank everyone who made their contributions to this thesis by providing their support and wisdom. I would like to thank my Advisor Prof. Sinha for his guidance, support and willingness to help at all times. I am thankful for Department of Mechanical Engineering and Science. This work would not be possible without contributions from my dear colleagues, and fellow group members Marc G. Ghossoub, Oksen T. Baris, Jun Ma, Dr.Myunghoon Seong, Krishna Valavala, Jyothi Sadhu, and Junghyun Lee. I would also like to thank my friends for their care and support.Special thanks should be attributed to Intel Research Council and the National Science Foundation through Grant No. NSF-CBET-09-54696-CAREER for funding my research. The micro-calorimeter presented in this paper was fabricated using clean-room facilities at the Micro and Nano- Technology Lab (MNTL) at the University of Illinois. Part of the work was also carried out in Frederick Seitz Materials Research Laboratory Central Facilities at the University of Illinois.

TABLE OF CONTENTS

LIST OF TABLES vi

LIST OF FIGURES vii

LIST OF SYMBOLS AND ABBREVIATIONS ix

CHAPTER 1 INTRODUCTION 1
1.1 Background 1
1.2 Thermal Energy Storage (TES) 2
1.3 Thesis Structure 8

CHAPTER 2 THEORY 9
2.1 Melting Enthalpy Enhancement 9
2.2 Melting Boundary Moving Calculation 12

CHAPTER 3 FABRICATION AND MEASUREMENT 15
3.1 Thin Film Deposition and Characterization 15
3.2 Micro-calorimeter Design and Fabrication 17
3.3 Calorimetry Measurements 20

CHAPTER 4 RESULTS AND DISCUSSION 28

CHAPTER 5 CONCLUSION AND FUTURE WORK 33

APPENDIX A DETAILED FABRICATION PROCESS 35

APPENDIX B MICRO-CALORIMETER DETECTION LIMIT . . . 40

APPENDIX C ERROR ANALYSIS 42

REFERENCES 45

LIST OF TABLES

1.1 Specific heat capacity of some common material 3
1.2 Data on solid state phase transition and melting entropy for a number of materials (adopted from [1]) 4
1.3 Thermochemical reaction candidate 6
1.4 Sorption Prototype 6

3.1 Instruments Specification 25

B.1 Dimensions and Properties of Calorimetric Cell 40

C.1 Values Needed for Error Estimation 43

LIST OF FIGURES

1.1 Specific enthalpy change for various thermophysical processes along with their typical temperatures highlighting the upper limit for capacitive thermal management at temperatures less than 400 K. 2
1.2 Chemical Storage and sorption storage classification. 5
1.3 Brief history of thermochemical energy storage. 5

2.1 Boundary position with constant temperature on side. 13
2.2 Constant surface heat flux model. 13
2.3 Volumetric heat capacity needed for a given heat flux. 14

3.1 Film thickness calibration 16
3.2 The refractive index n and the extinction coefficient of the fluorocarbon polymer for different film thicknesses measured using ellipsometry. 16
3.3 The surface profile of a metal heater with polymer deposited on top. 17
3.4 Schematic view of the micro-calorimeter from the top 18
3.5 The thermal resistance network for heat loss in the micro-calorimeter 19
3.6 Main Fabrication process 21
3.7 A schematic of the electrical circuit 22
3.8 A representative calibration curve for the reference and sample sensors between 300-400 K 23
3.9 Calibration curves for the same device before and after the post process 23
3.10 A representative transient temperature profile for an 18 nm polymer film. (Inset) Temperature rise during two successive pulses. Measurements are averaged over one thousand cycles to reduce noise. 24
3.11 A representative transient temperature rising rate with different fitting method 26
3.12 A representative raw volumetric heat capacity data 27

4.1 Measured volumetric heat capacities for different film thicknesses. The heat capacity, increases with temperature and decreases with film thickness and is independent of thickness for films thicker than 27 nm. 29
4.2 The Grüneisen parameter as a function of temperature for different film thicknesses as determined from the Debye Model 31

A.1 Pattern on mask 1 36
A.2 Pattern on mask 2 for backside etching 38

LIST OF SYMBOLS AND ABBREVIATIONS

T	temperature (K)
R	thermal resistance (K/W) or electrical resistance (Ω)
I	current (A)
A	area (m^2)
V	voltage (V) or volume (m^3)
t	time (s)
q	rate of temperature increase (K/ms)
G	Gibbs energy (J)
H	enthalpy (J)
S	entropy (J/K)
C_p	heat capacity at constant pressure (J/K)
C_V	heat capacity at constant volume (J/K)
M	molecular weight
k_B	Boltzman constant (J/K)
N_A	Avogadro constant (mol^{-1})
v	longitudinal speed of sound (m/s)
$X_{C/F}$	carbon fluorine ratio
σ	surface energy (J/m^2)
ρ	density (Kg/m^3)
θ_D	Debye temperature (K)
α	linear themal expansion coefficient

$\ddot{\gamma}$	Grüneisen parameter

Subscript

M	melting
b	bulk
R	reference
S	sample

CHAPTER 1

INTRODUCTION

1.1 Background

Capacitive thermal management is an attractive option for handheld electronic devices with power dissipation in the range of 1-10 W. A typical device consuming 10 W at peak usage requires a storage capacity of 144 kJ over a 4-hour usage period. Assuming a nominal volume of $10 \times 10 \times 1\text{cm}^3$, the required volumetric capacity is on the order of 1 GJ/m^3. Typically, only thermophysical storage mechanisms, involving either phase transitions or sensible heating, provide such large volumetric capacities. However, many of these options do not lie within the temperature range and the reliability constraints of electronics. Figure 1.1 plots the volumetric enthalpy change for various thermophysical methods of storage below 400 K. The figure facilitates a direct comparison between melting [2], and higher order phase transitions such as polymer glass transition [3], the electrocaloric effect [4], and the magnetocaloric effect [5, 6]. Amongst these, melting has the highest density and provides a wide choice of temperatures. The largest enthalpy change involves hydrated salts that are usually corrosive. Compared to hydrated salts, paraffins provide approximately 50% storage, liquid metals approximately 20% storage, and higher order phase transitions less than 10% storage. In addition to phase transitions, sensible heating provides thermal storage on the order of 10-100 MJ/m^3. Sensible heating requires large volumetric heat capacities and has typically been demonstrated in large-scale systems [7, 8], for example, solar energy system. Sensible heat storage, phase change storage and chemical storage are discussed in detail in Chapter 1.2.

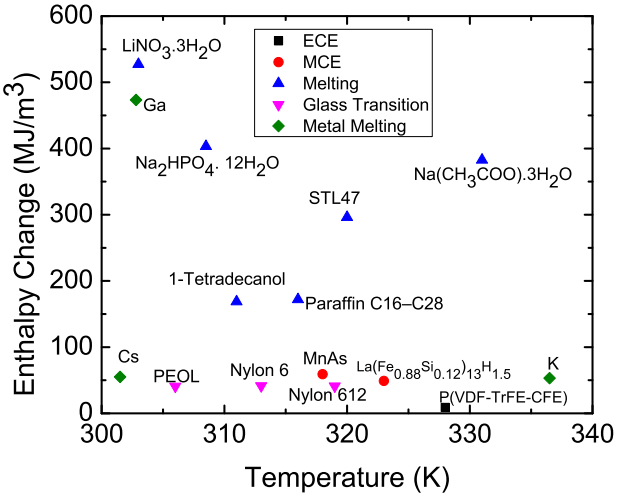


Figure 1.1: Specific enthalpy change for various thermophysical processes along with their typical temperatures highlighting the upper limit for capacitive thermal management at temperatures less than 400 K.

1.2 Thermal Energy Storage (TES)

The capacitive thermal management is one application of thermal energy storage (TES) technique. Generally speaking, there are three basic ways of thermal energy storage: sensible heat storage, latent heat storage and chemical storage [9]. Usually TES is widely used in large scale system.

1.2.1 Sensible Heat Storage

Sensible heat storage is the most common method, this process simply changes the material temperature without evolving any phase change or chemical composition change. Its principle is

$$\Delta H = \int_{T_0}^{T_1} C_p \, dT \tag{1.1}$$

where C_p is the heat capacity at constant pressure. According to Dulong-Petit rule, the molar specific heat of pure solid is $3R$, where $R = 8.31441$ J mol^{-1} K^{-1} is the molar gas constant.The heat capacity data of some common materials are listed below in Table 1.1 [1]. From Table 1.1, we can see water has relatively high energy storage density, thus water tank is usually used

Table 1.1: Specific heat capacity of some common material

Material	Specific Heat(J/(Kg · K))	Volumetric Heat Capacity(MJ/(m^3·K))
Brick	837	1.51
Wood	2390	1.67
Concrete	880	1.76
Glass	837	2.27
Steel	465	3.68
Water	4182	4.17

for building heating and cooling [10]. Thermal conductivity is an important factor that needs to be considered. For cooling, we usually require higher conductivity.

1.2.2 Latent Heat Storage

From thermodynamic view, based on Ehrenfest criteria, there are first-order and second or higher order phase change [11]. The first-order transitions happen at a constant temperature and are accompanied by latent heat, for example, melting and evaporation; on the other hand, there is no latent heat in second or higher order phase change, for example, glass transition. For glass transition, it actually happens at a temperature range, so we can calculate the enthalpy change during the phase transition. According to Ref. [1], for some solid material a phase change involves change in crystal structure, thus there is entropy change and enthalpy change below their melting temperature, this can also be considered as latent heat. Table 1.2(adopted from [1]) shows entropy change data for solid state. We can see [1], for some material, there is no big difference before and after the solid state transition, hence the entropy change is very small, like FeS; for some material, called paddlewheel materials[1] at temperature higher than the transition temperature, solid phase has a crystal structure in which one of the atomic species has an unusual vibrational amplitude or inter-site mobility, as a result the entropy change is high or even higher than the melting entropy change, like AgI, Ag_2S, Na_2SO_4, Ag_2SO_4. Those material might have the potential to be used at relatively lower temperature.

Ref [2] gives a detailed list of different phase change materials (PCM)

Table 1.2: Data on solid state phase transition and melting entropy for a number of materials (adopted from [1])

Material	Transition Temperature (°C)	Melting Temperature (°C)	Transition Entropy (J mol^{-1} K^{-1})	Melting Entropy (J mol^{-1} K^{-1})
FeS	138	1190	4.05	21.51
AgI	148	558	14.61	11.33
Ag_2S	177	837	8.86	7.01
Na_2SO_4	247	884	12.5	18.2
Ag_2SO_4	427	660	26.66	19.19
Li_2SO_4	577	860	29.2	7.9
$LiNaSO_4$	518	615	31.2	small

especially melting. The latent heat change density is usually higher than the sensible heat storage density. Paraffins, zeolite and salt hydrates like $NaSO_4 \cdot 10\,H_2O$ [12] are commonly used PCM.

1.2.3 Chemical Heat Storage

Thermal energy can also be stored in reversible chemical reaction. Heat is stored in the endothermic reaction of chemical compounds and during the reverse exothermic reaction heat is released. Thermochemical energy storage can be divided into two types: with and without sorption. And there are two different sorption types: adsorption and absorption. See Fig.1.2 (Adopted from [13]) for a detailed illustration. According to Ref. [13], adsorption is defined as surface phenomena that "an attachment of gas or liquid phase of a component to the surface of another substance"; absorption is used to describe the phenomena that a liquid or gas be absorbed by absorbent. For sorption system, we can define open and closed system which depends on whether the working fluid is in direct contact with the environment or not [14]. Thermochemical reaction energy storage is usually associated with solar energy application. People started to do research on the thermochemical energy storage since 1970s. Based on Ref.[15] and [16], I drew Fig.1.3 to simply show the history of thermochemical energy storage. People have done researches on many thermochemical reactions. To name a few, $NH_3+\Delta H \Leftrightarrow 1/2N_2+3/2H_2$ (Lovegrove,1999), $CH_3OH \Leftrightarrow CO+2\,H_2$)(Shiizaki,

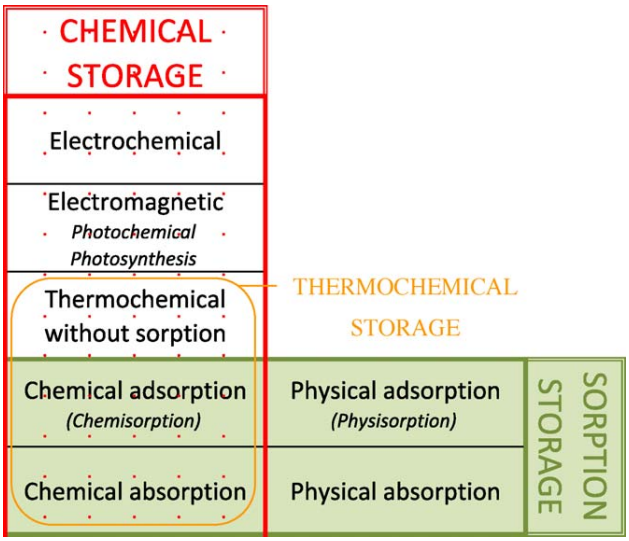


Figure 1.2: Chemical Storage and sorption storage classification. (Adopted from [13])

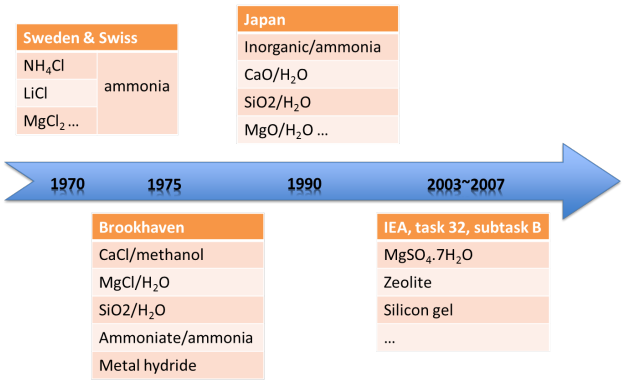


Figure 1.3: Brief history of thermochemical energy storage. Examples are from [15, 16]

Table 1.3: Thermochemical reaction candidate

Thermochemical Material	Solid ractant	Working Fluid	Energy Density (GJ/m^3)	Turnover Temperature °C
$MgSO_4 \cdot 7\,H_2O$	$MgSO_4$	H_2O	2.8	122
$FeCO_3$	FeO	CO_2	2.6	180
$Fe(OH)_2$	FeO	H_2O	2.2	150
$CaSO_4 \cdot 2\,H_2O$	$CaSO_4$	H_2O	1.4	89

Table 1.4: Sorption Prototype

Thermochemical Material	Energy Density (GJ/m^3)	Energy Density of prototype (GJ/m^3)	Temperature °C	System Type
LiCl salt, water, steel	0.91	0.306	80-100	closed absorption
NaOH,water	0.9	0.018	95	closed absorption
Silica gel, water, steel, copper	0.18	0.12	88	closed adsorption
Zeolite 13X	0.648	0.208	180	closed adsorption
Zeolite 4A	0.576	0.432	180	opern adsorption

2000)[17].For sorption system, see Table 1.3 ([18]) and Table 1.4 ([13, 16]) for a list of thermochemical reaction materials or sorption prototype that has been tested.

Some comments of the energy density for thermochemical energy storage: from the Table 1.3 and Table 1.4, the thermochemical material usually have higher heat storage density compared with sensible heat storage and latent heat storage, but the chemical method usually has gas phase involved which is not considered when calculating the heat density, and from Table 1.4 we can see when considered the total volume of the system, the actual energy density is low. The thermochemical storage also requires large system volume and is usually combined with solar systems. Other factors that limit the use of thermochemical storage include reaction reversibility, safety, reaction temperature etc.

1.2.4 TES Summary

To make use of the three TES methods, the ultimate problem is material. Overall, the best volumetric capacities are approximately two orders of magnitude less than the requirement discussed above for a 10 W device but can be promising for a 1 W design. Even for the latter case, the intrinsic thermal conductivity is too low for practical applications. Previous numerical [19] and experimental [20] work showed the necessity of a thermal conductivity enhancer in phase change material (PCM) [21, 22] based thermal management. Nanostructured materials provide a potential pathway for enhancing the storage capacity as well as reducing the thermal time constant. A high-surface, densely-branched scaffold [23]can provide highly conductive pathways while storage can occur in a material either encapsulated within or coated on the pathways. The small-size domain of the storage material provides an avenue for enhancement. For example, the melting temperature and enthalpy of metals becomes size dependent at the nanometer scale [24, 25]. The theory of melting enthalpy enhancement would be introduced in later part 2.1.

The Dulong-Petit law limits the heat capacity at constant volume near room temperature for most solids except those with very high Debye temperatures. The tunable parameter is then limited only to the atomic number density, which leaves little room for any dramatic improvement in storage density. As a first step toward such encapsulated/coated nanomaterials for thermal energy storage, we investigate the heat capacity of ultrathin (<20 nm) polymer layers that can be used as a coating on a high surface area metallic scaffold. Polymers are excellent candidates for electronics applications. They are typically inexpensive, non-corrosive, electrically insulating, and offer versatility in preparation. In this paper, we employ a plasma polymerization technique that yields ultrathin fluorocarbon polymer layers readily. The polymer layers are amorphous and do not undergo glass transition as typical polymers. We describe a MEMS fabricated micro-calorimeter designed to measure the heat capacity of polymer layers approximately 10 nm in thickness. Our measurements show an enhancement in the heat capacity at constant pressure as the film thickness decreases beneath a threshold. We model such phenomenon using the Debye theory of phonons. This work develops calorimetry and theory for characterizing and understanding the

heat capacity of ultrathin dielectric films with potential applications in the capacitive thermal management of electronic devices.

1.3 Thesis Structure

In Chapter 2.1, the theory of superheating and melting enhancement is explained. At the beginning of this project, we would like to use the nanostructure to achieve melting enthalpy enhancement. The polymer we used in the experiment does not undergo phase transition in the temperature range. This part indicates the potential of utilizing nano-confined structure to increase the heat storage of phase change material. In future work, we can choose some low-melting temperature material to test the nano-size effect. In section 2.2 melting moving boundary problem is solved for two different cases.

In Chapter 3, different aspects of the experiment: device design, fabrication, calibration and final calorimetry are discussed in detail. The structure of our device is originated from [26, 27, 28], but we made some modification to enhance the sensitivity. Though the structure is simple, the fabrication is really difficult due to the fragile membrane. Instead of using wet etch, we introduce a two-step dry etch to increase the yield ratio. The detailed fabrication steps including the photolithography masks are illustrated in Appendix A. The deposition method of the fluorocarbon polymer and its characterization is also discussed. The actual measurement has two main steps: device calibration and pulse measurement. The experiment details are discussed in section 3.3. The data reduction is explained in section 3.3.3.

In Chapter 4, we show the result of the volumetric heat capacity thickness dependence. This phenomenon is explained using the Debye theory of phonons. We claim that the thickness dependence might be directly related to the Grüneisen number. The possible error source is also discussed here.

In Appendix B, the estimation of calorimeter detection limit is explained. The error analysis is shown in Appendix C.

CHAPTER 2

THEORY

2.1 Melting Enthalpy Enhancement

Melting is a first order phase transition where the material transforms from the crystalline state to the liquid state. First order transitions are characterized by discontinuities in the derivative of the free energy. These first order discontinuities give rise to high energy changes in comparison to second order transitions which arise from discontinuities in first order derivatives. Statistical thermodynamics uses the Gibbs relationship to define changes occurring between the solid and the liquid. The Gibbs free energy change ΔG is

$$\Delta G = H - T\Delta S = 0 \tag{2.1}$$

where H is enthalpy, T is temperature and ΔS is change in entropy. A phase transition may occur when the change in Gibbs free energy becomes zero. However, equilibrium or free energies of the phases alone do not explain when melting occurs. Equally important is the thermodynamic mechanism by which the new phase first appears [29]. This thermodynamic mechanism can be initiated by a nucleation in the bulk, near an impurity or at the surface. Changes in volumetric enthalpy can be traced down to differences in material structure that alter nucleation mechanism or propagation of melting. We show in the following section how this may be exploited to achieve superheating.

The phenomenon of superheating describes an elevation in melting temperature. There are various methods of achieving superheating: using crystals with negative surface curvature [25], by drawing polymers [30], by limiting the solid/liquid interface kinetics etc. Among promising methods, embedding

crystal particles epitaxially in another material has been theoretically and experimentally studied, experimentally this can be achieved using sputtering technique to deposit layers with cohesive interfaces, the resulting degree of superheating can reach up to 100K for Al/Pb matrix [31].Fewer experiments of the superheating of thin films have been done, because heterogeneous nucleation of melt at various defects within the film and/or at the lateral free surface could not be avoided [25]. Though difficult, there are still some experimental observations. For example, thin Pb films confined epitaxially in Al by cold rolling and alternative DC sputtering depositions [32, 31].The maximum superheating degree for samples with 9nm Pb layers prepared use cold milling is about 60 K. Combine Nanda's [33] liquid-drop model and Guisbiers' [24] enthalpy relationship, we show the melting enthalpy would enhance due to superheating.

$$\frac{T_M}{T_{M,b}} = 1 - \frac{\beta}{6}\delta\left(1 - \frac{\sigma_c}{\sigma}\right) \tag{2.2}$$

Where T_M is the superheating melting temperature, and T_M,b is the bulk melting temperature; σ,$c$and σ are the surface energy of the confining material and the thin film separately. β is a function of surface energy and The shape factor δ is defined as surface area to volume ratio, for thin film, $\delta = 2/h$ where h is the film thickness. So if we choose confining material that has large surface energy, the surface energy ratio would be larger than one, hence superheating would occur.

Then use the method for derivation of free-standing particles [30] and modify it for thin films confined by other materials, we can get the relationship between superheating degree and enhanced melting enthalpy.The free enthalpy (or Gibbs free energy) of a nanostructure is considered to consist of two parts: the bulk free energy and the surface energy:

$$G = G_b + (A/V)\sigma_s \tag{2.3}$$

where G_b is the Gibbs free energy of bulk material, A is the surface area and V is volume.At a fixed temperature T, the Gibbs free energy difference between the liquid and the solid phases for a nanostructure is given by

$$G_l - G_s = G_{l,b} - G_{s,b} + (A/V)(\sigma_l - \sigma_s) \tag{2.4}$$

Here the subscript l and s denote liquid and solid state respectively. Substituting $G = H - TS$ will yield equation 2.4 in the following form:

$$\Delta H_M - T\Delta S_M = \Delta H_{M,b} - T\Delta S_{M,b} + (A/V)(\sigma_l - \sigma_s) \tag{2.5}$$

For confined thin film, the surface energy should be modified [25] as $\nu_l^* = \nu_l - x\nu_c$, $\nu_s^* = \nu_s - x\nu_c$, and x is the surface fraction covered by the substrate, when the surface is fully covered, $x = 1$, so rearrange equation 2.5

$$\Delta H_M - T\Delta S_M = \Delta H_{M,b} - T\Delta S_{M,b} + (A/V)(\sigma_l^* - \sigma_s^*) \tag{2.6}$$

At the superheating temperature, the particle begins to melt and the change in the Gibbs free energy becomes zero. Dividing Eq. 2.6 by the change in enthalpy of the bulk material, we get

$$\frac{T_M}{T_{M,b}} = 1 + (A/V)(\sigma_l^* - \sigma_s^*)\frac{1}{\Delta H_{M,b}} \tag{2.7}$$

If we If we substitute the bulk melting temperature, i.e. $\Delta H_{M,b} = T_{M,b}\Delta S_{M,b}$, equation 2.7 becomes

$$\Delta H_M - T_{M,b}\Delta S_M = (A/V)(\sigma_l^* - \sigma_s^*) \tag{2.8}$$

Substitute equation 2.7 into equation 2.8 and use $T_{M,b} = \Delta H_{M,b}/\Delta S_{M,b}$ and $T_M = \Delta H_M/\Delta S_M$, finally we can get

$$\frac{\Delta H_M}{\Delta_{M,b}} = \frac{T_M}{T_{M,b}} \tag{2.9}$$

This linear relationship indicates an increase in melting enthalpy by superheating. This shows that by using nano-structured material, we might store more energy during melting.

2.2 Melting Boundary Moving Calculation

In this section, I would briefly simulate how fast the melting boundary will move. This calculation would show how much PCM do we need to satisfy a certain time cooling. Ref. [19] provide detailed simulations of different situation. Suppose the PCM is paraffin. Its properties are as follows: melting enthalpy $\Delta H = 189KJ/Kg$, $\alpha = 1.08 \times 10^{-7}\mathrm{m}^2/\mathrm{s}$, $C_p = 2.13$ KJ/(kg K), T_m =316 K. In later part, I will calculate two cases: constant temperature on one side and constant heat flux on one side. The Ref [34] provides detailed derivation of the problems.

2.2.1 Constant Temperature On One Side

To simply the problem, consider a semi-infinite slab. Initially, the slab was at uniform temperature which is lower than the melting temperature. Suddenly, the $x = 0$ position is raised to a temperature T_0 higher than the melting temperature and keeps constant, the melting boundary position will move as follows:

$$S(t) = 2\lambda\sqrt{\alpha t} \tag{2.10}$$

where λ is the positive root of the equation 2.11

$$\lambda e^{\lambda^2}\mathrm{erf}(\lambda) = \frac{1}{\sqrt{\pi}}\mathrm{Ste} \tag{2.11}$$

here, Ste is Stefan number, which is defined as

$$\mathrm{Ste} = \frac{C_p(T_0 - T_m)}{\Delta H} \tag{2.12}$$

For paraffin, if $\Delta T = T_0 - T_m = 10$K, Ste=0.11; $\Delta T = T_0 - T_m = 40$K, Ste=0.44. Figure 2.1 shows how fast the boundary move for two different Ste situation.

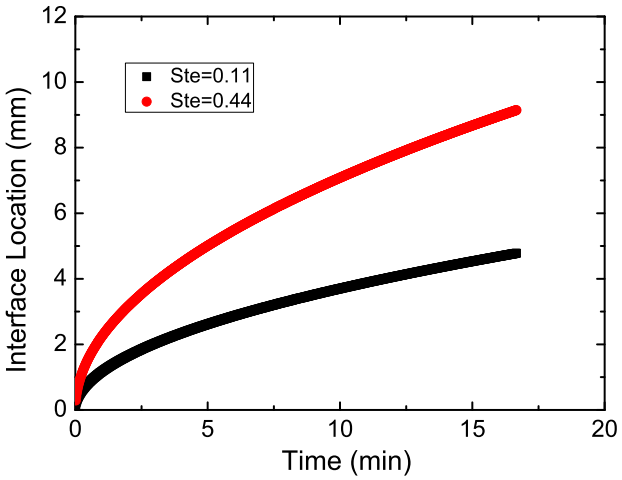


Figure 2.1: Boundary position with constant temperature on side. Ste=0.11 stands for $\Delta T = 10$K; Ste=0.44 stands for $\Delta T = 40$K.

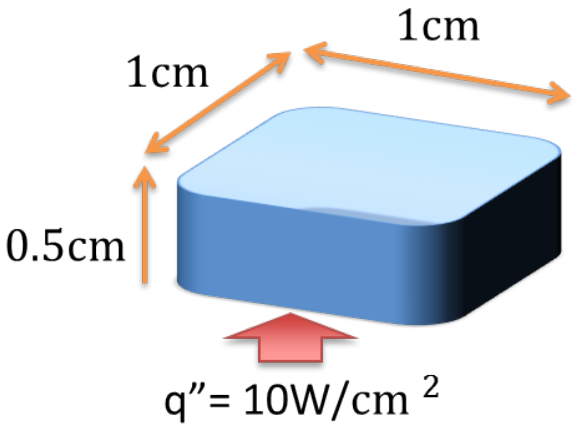


Figure 2.2: Constant surface heat flux applied to a constant volume PCM

2.2.2 With Constant Surface Heat Flux

In this part, we can assume the heat flux is 10 W/cm^2, and the PCM volume is 1cm $\times$ 1cm$\times$0.5cm,shown in Fig.2.2

The approximate solution for this problem is [34]. Quasi-steady assumption is used which means that the effects of sensitive heat are negligible relative to the latent heat.

$$s(t) = \frac{q_0''}{\rho \Delta H} t \tag{2.13}$$

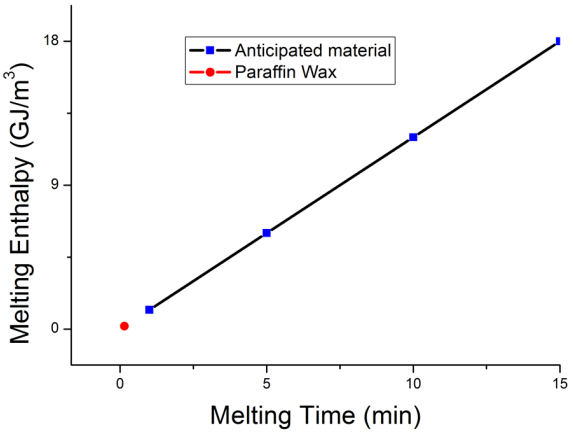


Figure 2.3: For a 1cm $\times$ 1cm$\times$0.5cm PCM, if we applied a constant heat flux on one side, we can calculate the anticipated volumetric heat capacity based on the time needed.

From Fig.2.3 we can see, if normal paraffin is used, the melting will finish in 9s, for such small volume, very large volumetric heat capacity material is needed.

CHAPTER 3

FABRICATION AND MEASUREMENT

3.1 Thin Film Deposition and Characterization

The material of focus is a ten nanometer scale thin fluorocarbon polymer film. We deposit such films in a reactive ion chamber (PlasmaLab RIE System) from a CHF_3 monomer gas flowing at 80 sccm, with a throttle pressure of 150 mTorr and RF plasma power of 80 W. In order to obtain a reference deposition time for a target film thickness, we first calibrated the film deposition rate [35]. Figure 3.1 shows that the deposition rate obtained from our calibration is approximately 8.4 nm/min and remains independent of film thickness in the range of interest. The low deposition rate enables relatively accurate growth of films with thickness less than 10 nm.

We used a variable-angle spectroscopic ellipsometer to measure the film thicknesses. Figure 3.2 shows the measured refractive index, n and the extinction coefficient, κ for different film thicknesses. Our measurements are consistent with previously reported data [36]. Ellipsometry errors increase significantly for films less than 10 nm thick. In the latter case, we used x-ray photoelectron spectroscopy to confirm the thickness measurements. We have provided extensive characterization of such films in our previous work [35].

We've tried different approaches to directly measure the polymer film thickness on the sample sensor: Alpha-Step Profilometers, Veeco Optical Profiler, AFM and etc. The main problem with these methods is that the silicon nitride membrane is fragile, even a tip touching would destroy the structure. For the optical profiler, because the film is transparent, the correct surface image cannot be obtained to extract the film thickness, see Fig.3.3. A dummy wafer is later used to determine the polymer thickness. To deposit polymer

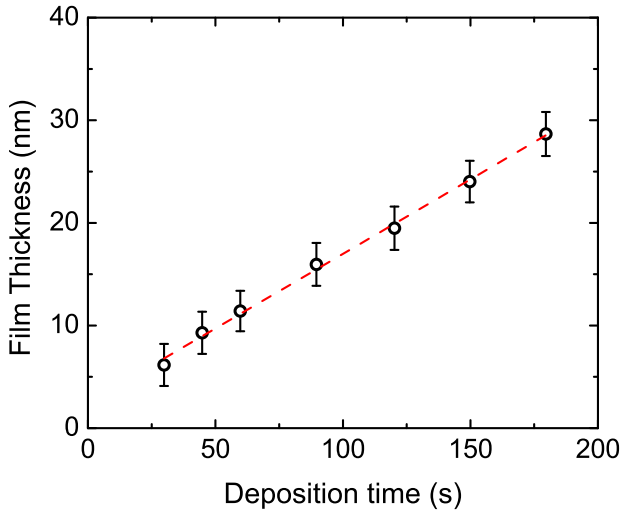


Figure 3.1: The film deposition rate is linear with time and allows 10 nm thin layers to be readily deposited.

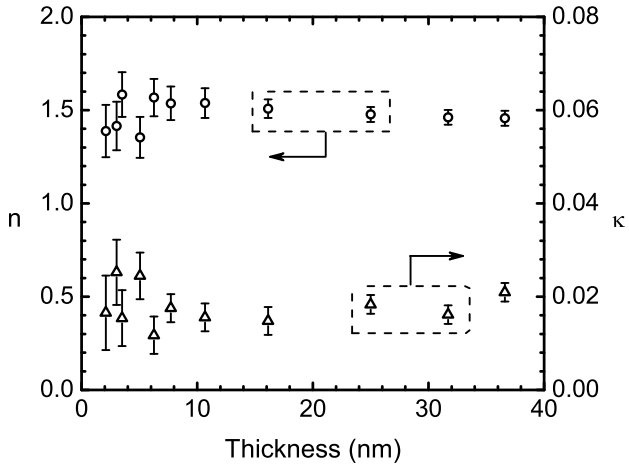


Figure 3.2: The refractive index n and the extinction coefficient of the fluorocarbon polymer for different film thicknesses measured using ellipsometry.

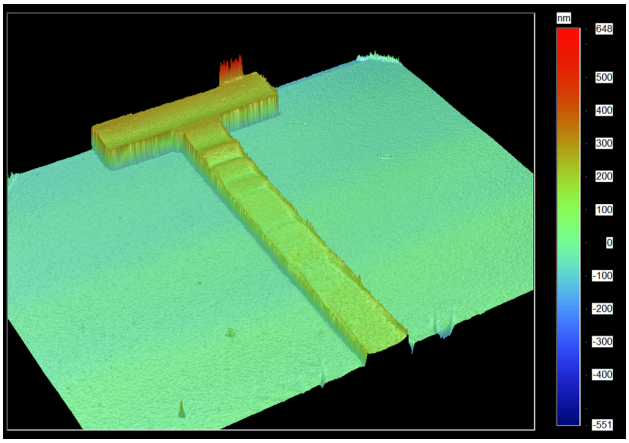


Figure 3.3: The surface profile of a metal heater with polymer deposited on top. The image is obtained by Veeco Optical Profiler.

on top of the metal heater, at first a shadow mask with heater shape through holes is used. The problem with this method is how to align the mask with the device properly and at the same time without breaking the device. Since the polymer which is not on top of the heater will not be heated, we only need to shield the contact pad during polymer deposition. Blue tape is utilized for this purpose because that it is easy to remove and would not leave residual.

3.2 Micro-calorimeter Design and Fabrication

In this section, we describe the design and fabrication of a micro-calorimeter for measuring the heat capacity of the above fluorocarbon polymer thin films. There are primarily three calorimetry approaches depending on the method of heating. The first involves stepwise increases in temperature; the second involves scanning the temperature at a constant or variable rate; and the third employs sinusoidal heating [37]. Of these three, the second is most widely used and commonly referred to as differential scanning calorimetry (DSC). This uses two identical heaters, one of which heats the sample while the other acts as a reference. Simultaneous measurements are necessary to obtain meaningful data. In particular, DSC is widely used in studying melting and glass transitions in polymers [37, 38]. The sensitivity of conventional desktop DSCs is typically insufficient to measure heat capacities of ultrathin

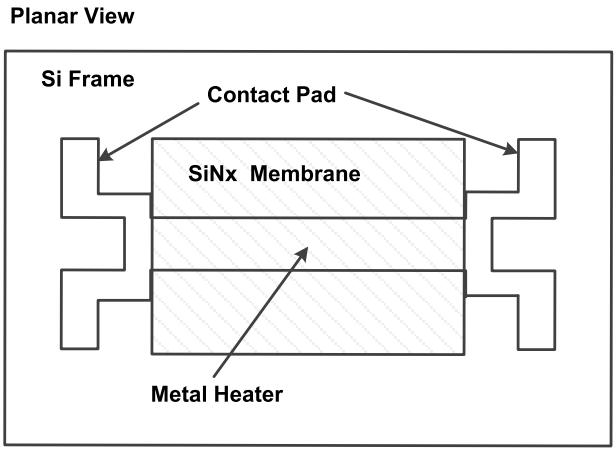


Figure 3.4: Schematic view of the micro-calorimeter from the top.

films. Instead, micro-fabricated calorimeters [26, 27] are used to measure polymer films down to 10 nm [39].

Figure 3.4 shows a schematic of the micro-calorimeter used in this work. A thin Aluminum strip 50 nm thick, 0.25 mm wide and 4 mm long, acts as the heater and the temperature sensor. The strip sits on top of a free standing silicon nitride membrane about 100 nm thick and with lateral dimensions 3 mm4 mm. The central part of the metal strip and the membrane beneath it form the calorimetric cell [28]. The thermal isolation due to the suspended membrane enables high temperature rise rates, on the order of 10 K/ms. This enables rapid heating by $\sim$ 100 K well within the thermal time constant of the device and allows adiabatic approximations in data analysis.

We reduced the size of the heater size from earlier reported designs [27] to further improve the thermal isolation from heater to ambient temperature. Figure 3.5 shows the thermal resistance network used to analyze heat flow between the heater and the ambient.

The total resistance is:

$$R = \left[\frac{1}{R_{polymer} + R_{poly-amb}} + \frac{1}{R_{mem} + R_{mem-amb}} \right]^{-1} \tag{3.1}$$

where $R_{polymer}$and R_{mem} are the thermal resistances of the polymer sample and the membrane beneath the metal heater respectively. The ambient to

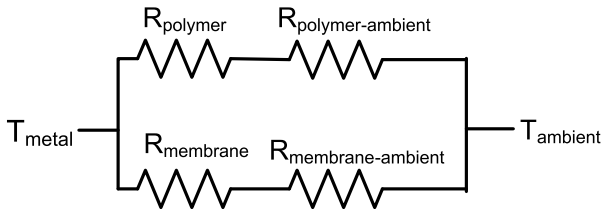


Figure 3.5: The thermal resistance network for heat loss in the micro-calorimeter.

polymer, and the ambient to membrane thermal resistances are $R_{poly-amb}$ and $R_{mem-amb}$ respectively and include contributions from conduction through air and radiation. The dimensions of the calorimeter are chosen such that the ratio of the thermal resistance through the polymer to the total thermal resistance is of the order of 10^{-6}. For the membrane to ambient thermal resistance, we can both consider the conduction to air and radiation. The resistance of air conduction can be calculated as follows [40]

$$R_{air} = \left[\frac{1}{2k_{air}(D_{eff})}\right] \tag{3.2}$$

The D_{eff} in Eq.3.2 is effective diameter, which can be estimated by the surface length l and width w.When the pressure is very low, radiation dominates.

$$D_{eff} = \sqrt{\frac{4lw}{\pi}} \tag{3.3}$$

The detection limit of the micro-calorimeter described above depends on the sensitivity of the current and voltage measurements. We use Keithley 6221 DC/AC current sources to provide both the DC and the pulsed currents and a National Instrument PCI-6259 DAQ card to measure the voltages. The smallest voltage change detected by the DAQ is 112 μV in the 10V range. In typical experiments, the pulsed current is approximately 28mA. Based on our calibration, the product of resistance and temperature coefficient, dR/dT for the metal film is $0.02\ \Omega/K$. The minimum temperature increment that can be detected is approximately $\Delta T_{min} = \frac{\Delta V}{I}\frac{1}{dR/dT}$. Using the calorimeter dimensions and physical properties [41, 42], we estimate the heat capacity of

the calorimetric cell to be $1.7\ \mu J/K$. Combining the minimum detectable temperature change and the heat capacity, we estimate the minimum measurable enthalpy change to be $0.3\ \mu J$. The calculation detail is later discussed in Appendix B.

The fabrication of the calorimeter proceeds as follows. We use atomic layer deposition to deposit a layer of Al_2O_3 on top of a double-sided polished silicon wafer. The alumina acts as an etch stop for later processing. An STS Mixed-Frequency Nitride PECVD System deposits a second layer of 100 nm thick SiN_x on top of the alumina. We lithographically pattern the silicon wafer, deposit aluminum for the heater using a CHA SEC-600 E-Beam/Thermal Evaporator and perform a lift-off to obtain the metal strip. Prior to patterning the back side of the wafer and releasing the membrane, we attach the wafer to a second carrier wafer. Releasing the membrane is the most difficult step in the fabrication process due to the 100 nm membrane thickness necessary for the calorimetry. We avoid wet etching with KOH for better process yield. Instead, we use an ICP-RIE process to etch most of the silicon and then separate the process wafer from the carrier. A final dry etching with XeF2 removes the remaining silicon to leave a free standing nitride membrane. This two-step etching achieves relatively high yields. Figure 3.6 (a) summarizes the micro-fabrication process. A fabricated DSC device with two membranes is shown in Fig. 3.6 (b). We deposit a film on one of the membranes prior to the measurement while another membrane serves as reference. The polymer film also deposits concurrently on a dummy wafer for use in ellipsometry. Fabrication recipe is shown in Appendix A.

3.3 Calorimetry Measurements

During the measurement, a pulsed current applied through the metal strip heats the metal and the polymer on top of it. Transient 4-probe resistance measurements provide the temperature rise with time using a resistance-temperature calibration curve. The same metal strip functions both as a heater and a temperature sensor, similar to most micro-fabricated thermometry platforms. The device is designed for a thermal time constant of $\sim$ 30 ms. A heating rate leading to a rate of temperature rise exceeding 10

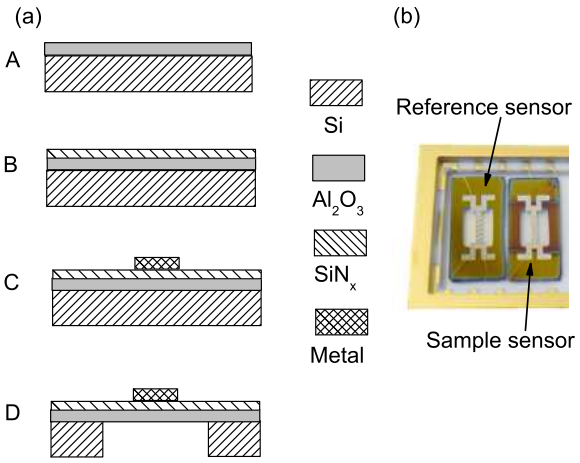


Figure 3.6: (a) Schematic of the fabrication process: (A) Al_2O_3 deposition by ALD to serve as the etch stop for later backside etching (B) SiN_x deposition by PECVD (C) heater definition by metal evaporation and lift-off (D) backside silicon etching by ICP-RIE and XeF_2. (b) A finished device showing the reference and sample calorimeters..

K/ms is necessary to achieve near-adiabatic conditions assumed in the analysis. Normally, the temperature rising rate can be as high as 40 K/ms. Under adiabatic heating without any heat diffusion, we may assume a simple relationship between the voltage across the strip, V, the current, I, the temperature, T and the heat capacity of the structure C_p

$$V(t)I(t)dt = C_p(T)dT \tag{3.4}$$

3.3.1 Calibration

A precise calibration is the key of this experiment. The calibration and DSC measurements are performed in a Janis ST-100 cryostat under 14 18 mTorr pressure to reduce convective losses and achieve adiabatic conditions. At the beginning we were using mechanical pump, later a turbo pump is used, so high vacuum can be reached. Figure 3.7 illustrates the circuit used in the calibration and the measurements. The resistance-temperature calibration is especially important in micro-calorimetry. A pre-calibration step involves increasing the temperature inside the cryostat from 300 K to

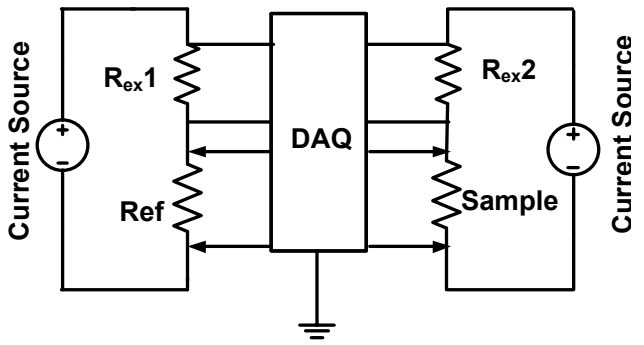


Figure 3.7: A schematic of the electrical circuit. The label "Ref" indicates the reference device and "Sample" indicates the device with the deposited polymer. Rex1 and Rex2 are two known resistors used to measure the applied current. A DAQ card measures voltages.

400 K at increments of 10 K to obtain a reference curve. The heater is then annealed by applying pulsed currents similar to those used subsequently in DSC measurements. Typically, this pulse is repeated more than 3000 times to anneal the metal and obtain a stable response [43]. Without the "burn-in", the calibration curves show significant variations in different runs. After the "burn-in", we obtained repeatable calibration curves using a 1 mA DC current. Figure 3.8 shows the calibration curves for a typical reference and a polymer-coated device. The small difference in the curves, arising from variability in fabrication, is one of the main sources of error.

The figure 3.9 below shows the calibration curves change before and after the post process (annealing and burning) step.

To obtain good calibration curves, high sensitivity and precision instrument is preferred. Lock-in amplifier is a better choice compared to the DAQ 6259. The basic assumption of calibration is that the device reaches balance state with the environment (here the cryostat chamber), so before taking any points, we should wait until the temperature change is less than 0.1K in 10 minutes.

3.3.2 Actual Measurement

The DSC measurements use a pulsed current at 1 Hz and a duty cycle of 1%, to provide 10 ms of heating per cycle. The duration of the heating is

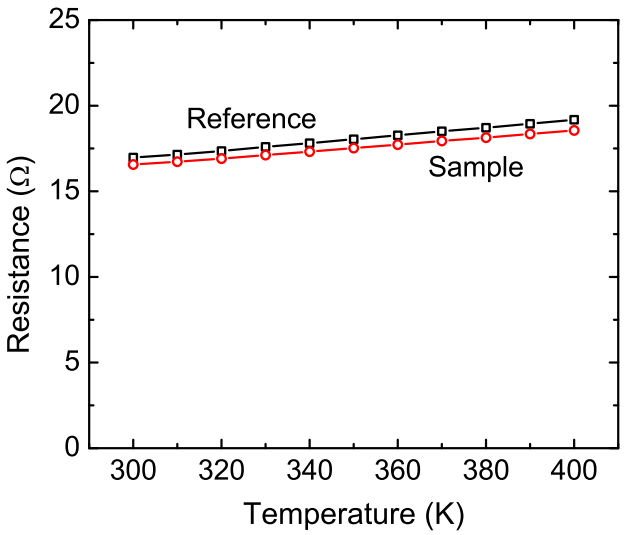


Figure 3.8: A representative calibration curve for the reference and sample sensors between 300-400 K.

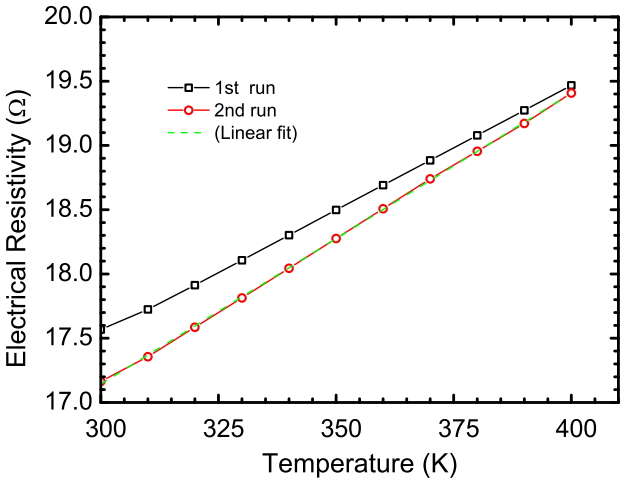


Figure 3.9: A representative Calibration curves for the same device before and after the post process. Usually the resistance would drop a little after annealing and behaves stable in later test.

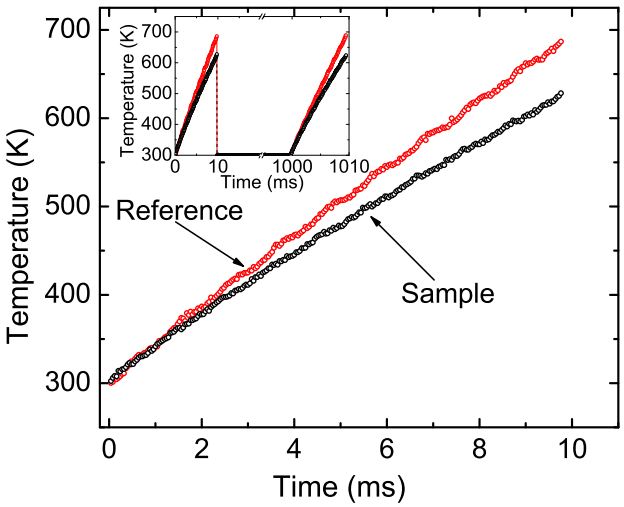


Figure 3.10: A representative transient temperature profile for an 18 nm polymer film. (Inset) Temperature rise during two successive pulses. Measurements are averaged over one thousand cycles to reduce noise.

smaller than the thermal time constant of the system, approximately 30 ms. To obtain the thermal time constant, I added a small DC offset to the pulse, so a resistance or temperature decaying curve can be plotted. Then fit the curve exponentially to extract the time constant. The 990 ms idle time is sufficient to completely cool the calorimetric cell to the ambient temperature. A LabView program triggers the two current sources simultaneously and records data. The inset of Fig. 3.10 shows the temperature rise in the reference and the sample devices during a single heating pulse.

Our measurements use a sampling rate of 100 KHz. The memory and the bandwidth available in the DAQ limit the overall rate. We use eight channels simultaneously to measure four voltages. Since the DAQ 6259 has a maximum bandwidth of 1.2 MHz, the sampling rate per channel is limited to $\sim$ 100 KHz. To manage memory usage, we average over 4 data points to obtain 25000 data points per second per channel. We further note that the voltage limit of each channel must be larger than the compliance voltage of the current source. The differential mode of the DAQ should be chosen. At first, we just assumed the current value is the same as set value of the current source. Later I realized that the actual current value must be measured especially we are using a pulse current. Three possible ways are available to measure the current: Agilent 34401A $6\frac{1}{2}$ Digit Multimeter, Keithley 6485 Picoamme-

Table 3.1: Instruments Specification

Instrument	Accuracy	Drawback
Digital multimeter	I≤10 mA: ±(0.0005%+0.001 mA) I ≤ 100 mA: ±(0.01%+0.004 mA)	Maximum reading speed is 1000/s
Picoammeter	I≤2 mA: ±(0.1%+1 nA) I ≤ 20 mA: ±(0.1%+0.001 mA)	Maximum range is 20 mA; maximum reading speed is 1000/s
DAQ 6259	±10 V range: 0.0184%+83 μV	accuracy depends on the external resistor

ter, and using DAQ 6259 to measure the voltage across an external resistor. The specification of different instruments are listed in Table 3.1. The main drawbacks of direct current measurement with multimeter or picoammeter is the low reading speed. So the only choice is use DAQ 6259 to measure the external resister voltage to obtain the current value. By choosing proper resistor, we can reduce the measurement error. At the same time, the external resistor should not be too larger than the device resistance. Finally two 100 Ω external resistors are used.

3.3.3 Data Reduction

The raw data from the experiments include the currents through the reference and sample heaters,$I_R(t)$and $I_S(t)$, and the voltages across the two sensors,$V_R(t)$ and $V_S(t)$. We briefly discuss the data extraction procedure next. We point the reader to Ref [28] for a detailed discussion on the analysis. Rewriting Eq. C.1 for the reference and the sample,

$$V_R(t)I_R(t)dt = C_{p,R}(T_R)dT_R \tag{3.5a}$$

and

$$V_S(t)I_S(t)dt = [C_{p,S}(T_S) + C_{p,X}(T_S)]dT_S \tag{3.5b}$$

where $C_{p,R}$,$C_{p,S}$ and $C_{p,X}$ are the heat capacities of reference sensor, the

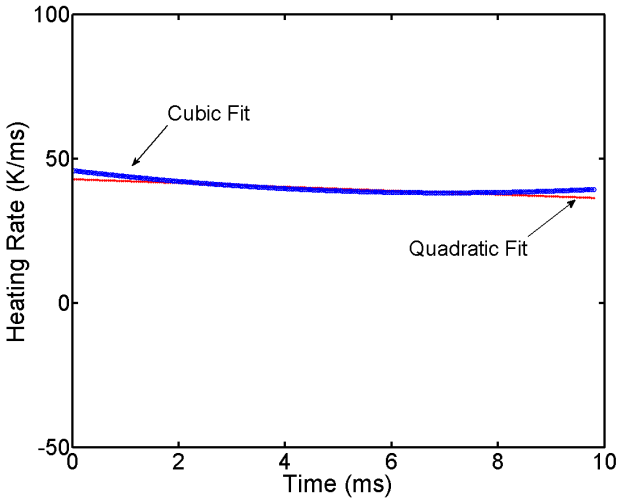


Figure 3.11: A representative transient temperature rising rate with different fitting method. The cubic and higher order fit shows an unphysical curve so a quadratic fit is used instead

sample sensor and the polymer respectively. Based on the assumption that the reference and sample sensor have the same heat capacity, subtracting Eq.3.5a from Eq. 3.5b yields

$$C_{p,X}(T_S(t)) = \frac{V_S(t)I_S(t)}{dT_S/dt} - \frac{V_R(t)I_R(t)}{dT_R/dt} \tag{3.6}$$

Denoting the rate of temperature increase as

$$q(t) = dT/dt = \frac{dR(t)/dt}{dR(t)/dT} \tag{3.7}$$

the heat capacity of the sample can be expressed as [28]

$$C_{p,X}(T_S(t)) = \frac{V_R(t)I_R(t)}{q(t)} \times \left[\frac{V_S(t)I_S(t)}{V_R(t)I_R(t)} \times \frac{1}{q_S(t)/q_R(t)}\right] \tag{3.8}$$

Since $q(t)$ involves taking derivatives, these terms introduce significant noise as discussed in previous work [28]. To reduce the noise, we fit a curve to the raw temperature rise profile shown in Fig. 3.10 and use the fit to extract derivatives. We find that quadratics fit the transient profiles well. See figure 3.11 This step helps smooth the extracted data. We discuss the heat capacity data for films of different thicknesses in the next section.

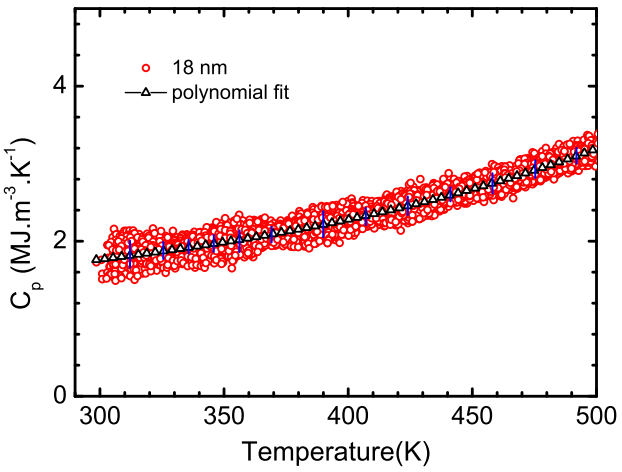


Figure 3.12: A representative raw volumetric heat capacity data. The small blue vertical line indicates the standard deviation range. Later we use the regional statistics function in Origin 8.5 Pro to extract the standard deviation

Because we usually have 1200 pulses for each measurement, each pulse would give a specific heat capacity curve, we then superimpose as all the curve as shown in Fig.3.12 together and then fit a curve out of it. From the figure we can see that all the raw data show the same trend and the standard deviation is within 10% of the average value. The small blue vertical line is used o demonstrate the standard deviation, later we used the regional statistics function in Origin 8.5 Pro to extract the actual value. We then compared this standard deviation with the calculated error (see Appendix), choose the larger one to be our measurement error. According to Ref.[28], using an idle experiment can further improve the accuracy and precision of the calorimetry. Basically, we need to do a pulse measurement on the two sensors before polymer sample is deposited. After that, deposit polymer on one heater and then redo the same measurement. The reason we did not do this correction was due to the fragile membrane. If this correction can be done, the accuracy of the experiment would be improved.

CHAPTER 4

RESULTS AND DISCUSSION

Figure 4.1 plots the measured volumetric heat capacities for polymers of thicknesses in the range 12 to 60 nm, as a function of temperature. The error bars account for noise in the measurement as well as uncertainties in determining the film thickness and the heater temperature. We find that the volumetric heat capacity shows an increase with increasing temperature and decreasing film thickness. The measured heat capacity for the 60 nm thick film is slightly larger than the 27 nm thick film at temperatures above 400 K. We attribute this difference to errors in measuring the film thickness accurately due to surface waviness in thicker films. We expect little difference between these two films in general. However, the increasing heat capacity trend with lower thicknesses is evident in the 12 nm and 18 nm films.

The heat capacity includes contributions not just from the bulk of the film but the film's free surface and its interface with the metallic heater. While surface related effects should increase with decreasing thickness, it is not clear that this should necessarily lead to an increase in heat capacity. In order to explore this behavior, we start with the Debye model [44] and estimate the lattice contributions to the heat capacities of the fluorocarbon films as

$$\frac{C_V}{V} = 9\left(\frac{N_A}{M_{film}}\right) k_B \rho \left(\frac{T}{\Theta_D}\right)^3 \int_0^{\Theta_D/T} \frac{x^4 e^x}{(e^x-1)^2}\, dx \tag{4.1}$$

where $M_{film}$is the molecular weight and ρ is the density of the fluorocarbon film. Here, k_B and N_A are the Boltzmann and Avogadro constants respectively. In our previous work [35], we have shown that the chemical composition of plasma polymerized CHF_3 varies with thickness for thicknesses below 25 nm. The carbon to fluorine ratio $X_{C/F}$ and the average coordination number increase with decreasing film thicknesses. We use the previously measured carbon to fluorine ratios to obtain the number average molecular weight of

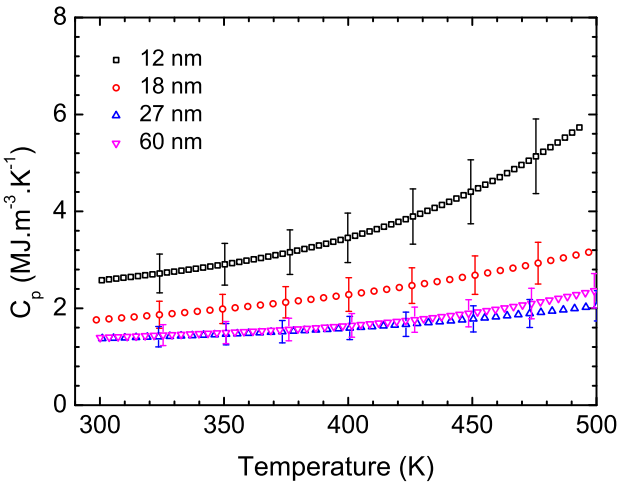


Figure 4.1: Measured volumetric heat capacities for different film thicknesses. The heat capacity, increases with temperature and decreases with film thickness and is independent of thickness for films thicker than 27 nm.

the films as a function of thickness as

$$M_{film} = \left(\frac{X_{C/F}}{1 + X_{C/F}}\right) M_c + \left(\frac{1}{1 + X_{C/F}}\right) \tag{4.2}$$

where M_c and M_F are the molecular weights of carbon and fluorine respectively. The Debye temperature,Θ_D in Eq.4.1 is given by

$$\Theta_D = \left(\frac{\hbar}{k_B}\right) v \left[6\pi^2 \left(\frac{N_A}{M_{film}}\right) \rho\right]^{1/3} \tag{4.3}$$

where v is the speed of sound in the fluorocarbon. We have previously determined [35] the speed of sound as function of film thickness and found this to increase with decreasing film thickness. The volumetric heat capacity at constant pressure accounts for thermal expansion and is expressed as follows:

$$\frac{C_p}{V} = \frac{C_V}{V} + 9\alpha^2 v^2 \rho^2 T \tag{4.4}$$

In the equation above, $\alpha$is the linear thermal expansion coefficient of the thin film and can be expressed in terms of the Grüneisen parameter γ as:

$$\alpha = \frac{\gamma}{3v^2\rho} \frac{C_V}{V} \tag{4.5}$$

The volumetric heat capacity at constant pressure thus becomes

$$\frac{C_p}{V} = \frac{C_V}{V}\left[1 + \frac{\gamma^2}{v^2\rho}\frac{C_V}{V}T\right] \tag{4.6}$$

Equation 4.6 shows that the volumetric heat capacity at constant pressure depends on mass density, the speed of sound and the Grüneisen parameter. The temperature dependence observed in Fig. 4.1 can result from dependencies in each of these three properties. The dominance of any one property is not clear from Eq.4.6. To resolve this issue, we first fit the temperature trend in the data using the film density and the speed of sound as temperature dependent parameters while keeping γ constant. This results in an unphysical increase in each property with temperature. Therefore, we discount changes in density and the speed of sound as being responsible for the observed trend.

In order to proceed with Eq.4.6 , we need an estimate of the mass density. We estimate the film density by fitting the Debye model heat capacity (Eq. (4.6)) to the measured C_p at 300 K for the thickest film and assume the same for thinner films across the full range of temperatures under consideration. We use the measured speed of sound and set the Grüneisen parameter to unity. We have previously measured [35] the mass density of similar fluorocarbon films that are capped by a thin layer of aluminum. The film density was relatively constant for films of different thicknesses with an uncertainty of around 15%. We note that the Grüneisen parameter for these films has not been measured. However, measurements on tetrahedrally bonded amorphous solids [45] such as our fluorocarbon films and molecular dynamic simulations on amorphous Si [46] show that the Grüneisen parameter is close to unity at room temperature. Thus, we set the Grüneisen parameter to unity for the thickest film. We note that the Grüneisen parameter of polymeric solids has values in the range 3 to 9 for polymeric glasses [45, 46, 47, 48]. However, we expect lower values of γ in our samples since these are amorphous and highly cross-linked.

Having estimated the mass density using the data for the thickest films, we proceed to estimate the Grüneisen parameter for the other films using the previously measured speed of sound. Marching along the curve in temperature,

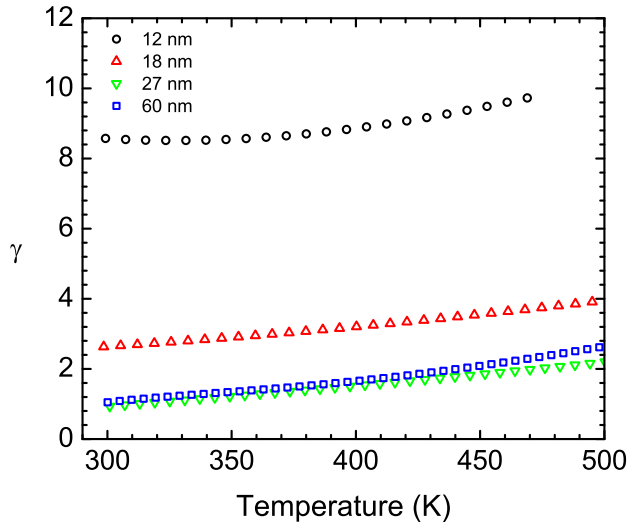


Figure 4.2: The Grüneisen parameter as a function of temperature for different film thicknesses as determined from the Debye Model.

we calculate the change in the Grüneisen parameter with temperature.As discussed above, changes in density or the speed of sound cannot account for the observed trend in heat capacity with temperature.

Figure 4.2 shows that the normalized Grüneisen parameter as a function of temperature increases linearly with temperature, consistent with previous measurements on other polymeric glasses. The rate of change of γ with temperature is largest in the thinnest films. While this appears as a size dependence in Fig. 4.2 , we argue that the difference in $d\gamma/dT$ actually arises from a difference in chemical composition and not from changes in the physical dimensions.

We have previously reported that the carbon-to-fluorine ratio increases with decreasing film thickness [35]. As the film becomes carbon rich, we expect the average bond anharmonicity to also increase. The C-F bond is highly polarized, and is shorter and stronger than the C-C bond [49]. The bond dissociation energy progressively increases as the number of fluorine atoms attached to a carbon atom increases. Thus, we expect a carbon rich film to be more anharmonic than a fluorine rich film. The sharper increase in the Grüneisen parameter with temperature for the thinner and carbon rich films reflects this behavior.

Our experiments suggest that the Grüneisen parameter provides an addi-

tional tuning parameter for enhancing the thermal storage density in sensible heating based methods. Here, amorphous and glassy materials are a better candidate than crystalline materials since the available range of Grüneisen parameters is larger. However, consistency in the preparation method is a pre-requisite for harnessing this effect in thermal storage. Previous work [50, 51, 52, 53] on amorphous silicon has shown the Grüneisen parameter shows a large dispersion in values depending upon the preparation of the sample. The dispersion arises from volume driven internal strain that can vary depending on the preparation method. In terms of chemistry, the intrinsic value of the Grüneisen parameter depends on the stretching character of the chemical bond. A large bond-stretching character rather than a large bond-bending character favors large values of γ [54].

CHAPTER 5

CONCLUSION AND FUTURE WORK

In conclusion, we have designed and fabricated micro-calorimeters capable of measuring the heat capacity of nanometer thin films. Measurements on fluorocarbon polymer films as a function of thickness show a three-folds increase in the volumetric heat capacity when the film thickness diminishes from 27 nm to 12 nm. Using a Debye model of phonons, we attribute this increase to an increase in the Grüneisen parameter. This increase arises from subtle changes in the film composition with thickness. Thinner fluorocarbon polymer films are relatively carbon rich, which promotes their anharmonicity. The overall increase in heat capacity suggests that chemical compositional changes can potentially yield enhancements in thermal storage density for sensible heating based storage. This can potentially lead to a viable materials system for capacitive thermal management in electronics. This work advances the understanding of physical processes underlying high density thermal energy storage.

From previous calculation in 2.2, we can see that the main drawback of the capacitive thermal management for electronic devices is the volume limit. Even if we can achieve very high volumetric heat capacity, it can still only support very short time cooling. This method can be a useful backup or assistant system for cooling in handheld devices. Another issue with the capacitive cooling is that the high volumetric material usually have small heat conductivity. One solution might be embedded high conductive carbon nanotube or other method to enhance the thermal conductance, although this would bring cost consideration.

Our investigation is only the first step in this direction and future work needs to expand the range of materials. In future work, we can choose different type of materials that can be deposited properly on top of the metal heater. In this work, the fluorocarbon polymer did not undergo a

phase transition, we can further test some low melting point materials to verify our theory about the melting enthalpy enhancement. We can also try different methods to enhance the thermal conductance and build laboratory prototype to test its performance.

APPENDIX A

DETAILED FABRICATION PROCESS

1. RCA clean. Because the we need to do back side etching, so double-sided polished wafer is needed. A thickness of about $300\mu m$ is proper for our fabrication. The silicon doping level and type is not so important. Remember to wear black chemical gloves, face shield and apron when dealing with HF solution.

Detailed process:

- H_2SO_4: H_2O_2=4:1, 90°C 10min. Dump Rinse (standard 6 cycles) OR overflow rinse for 5 minutes (if at wbgeneral)This step is used for organic removal
- 5:1:1 H_2O:H_2O_2:HCl 70°C for 10 minutes.This step is for metal removal
- Dump Rinse (std 6 cycles) OR overflow rinse for 5 minutes (if at wbgeneral).
- 50:1 HF dip for 15 - 30 seconds to remove the native oxide

2. Al_2O_3 deposition

Using Atomic Layer Deposition System (ALD) to deposit Al_2O_3 on silicon wafers, operating temperature is 250°C; the thickness is about 200 Å (250 cycles × 0.9 Å/cycle). It would be better to measure the thickness using Ellipsometer after deposition. Then sputter PR to protect the top Al_2O_3 layer (normal procedure). Use HF solution to remove the SiO_2 of the backside in order to remove the ALD window which is inevitable in the ALD deposition but would affect the later backside etching. Because the etching rate is very fast, first etch 5 10 seconds to check.

3. SiN_x deposition

Using STS PECVD with mixed frequency recipe, the deposition rate is

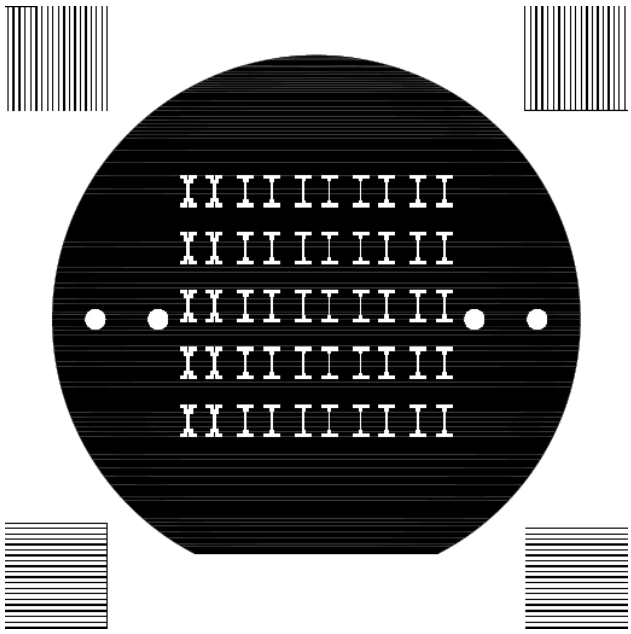


Figure A.1: Mask 1.

around 14 nm/min, remember to measure the wafer stress before and after the deposition. The Platen Temperature is 300 °C (Lower Electrode) and the Showerhead(Upper electrode) temperature is 240 °C . Chamber pressure is 900 mTorr, Nitrogen flow is 1960 sccm. 40 sccm SiH_4 and 50 sccm NH_3 are used for deposition. The RF power is set to be 20W HF(13.56Mhz) for 6 seconds followed by 20W LF(380kHz) for 2 seconds. This mixed frequency method can produce membrane with lowest film stress.

4. Pattern and develop (Mask #1).

Detailed process:

- HMDS, 4000rpm, 35s. HMDS is carcinogenic, remember to wear mask.
- Spin coat photoresist (PR) S1813, 35s 4000 rpm.
- Soft bake on the hot plate (110°C) for 1min 30sec
- Expose 12 sec (12 × 7.5 mW) using Quintel aligner
- Develop pattern with AZ300 MIF for 1 min
- Inspect pattern quality under microscope. Apply another 2 minutes O_2 descum to remove the PR in pattern region

5. Aluminum deposition (using CHA SEC-600 E-Beam/Thermal Evaporator)

The E-beam evaporator can deposit uniform metal film. The aluminum sticks to silicon very well, so $10^{-}6$Torr pressure is enough. This usually takes one and half hours to pump down. For CHA evaporator, a 37% power level would provide $1 \sim 2$ $\mathring{A}$/min deposition rate. Sputtering can also be used for the metal deposition. A metal layer of 50 nm is used for the heater.

6. Lift off: acetone bath for 10 min or less (keep observing), and then sonication.

7. Pattern backside and develop using AZ 400T (4:1). And then stick to the carrier wafer.

Before spin coat PR on the backside, we should coat the top side with PR following the normal PR S1813 recipe. The backside pattern is later used for backside though etching, so thicker PR is required,here we used AZ4620. To stick the wafer to a carrier wafer, we also used the normal PR spin coat procedure and then stick them together. The carrier wafer is also used to protect the top pattern. Actually, the crystal wax might be better choice for the sticking process because it is relatively easy to remove. To finish the back side pattern, a back side aligning must be performed with the IR light of the Quintel system.

Detailed process for thick PR:

- HMDS, 4000rpm, 35s;
- PR (ZA4620), 30s 3000 rpm, the PR thickness would be about 8 μm
- Soft bake on the hot plate (110°C) for 10 min
- Expose 65 sec (12×7.5 mW) using Quintel aligner
- Develop pattern with AZ400K (1:4 solution)

8. Etching using ICP RIE (STS Advanced Silicon Etcher). The ICP machine uses Bosch process to produce vertical side walls.

The detailed recipe is as follows:

- Etch step: 130sccm SF_6 + 13scccm O_2(12 + 0) pressure is 40mT, RF

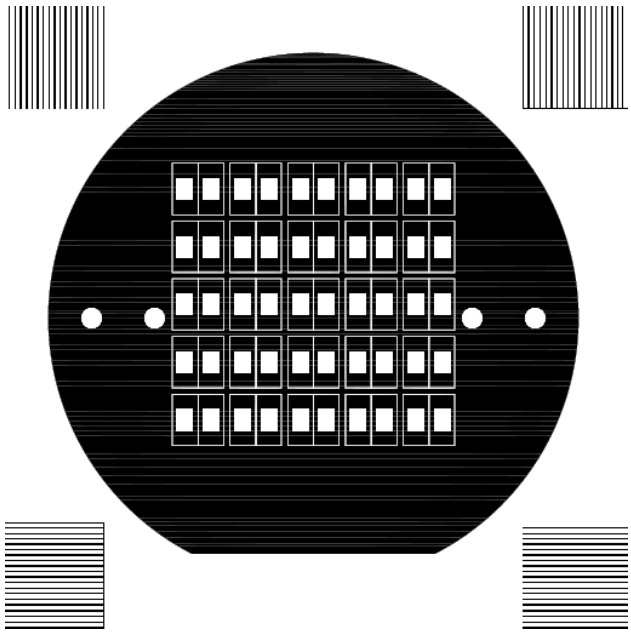


Figure A.2: Mask 2 for backside etching.

coil 600W, platen 12W

- Deposition step: 78 scccm C4F8(8 + 0), pressure is 22mT, RF coil 600W, platen0W.

With this recipe, the silicon etching speed is about $3 \sim 4\mu m/min$. Normally I used a $300\mu m$ wafer, so after about 70 minutes, the etching process should be carefully checked every one or two minutes. The etching time should be controlled that after this step, only very thin silicon is remained

9. Acetone bath or PR stripper bath (better) to release the sample wafer from the carrier wafer. This process time varies from 1 day to 3 day depends on the PR adhesion layer, PR stripper is a better choice though no test has been done with PR stripper. This step needs great caution due to the fact that all the membrane are almost exposed and they are very fragile.

10.Etching with XeF_2 to release the free standing membrane.

One thing to notice here is that, due to the load effect, the etching rate becomes really slow if the whole wafer is being etched, it would be better if you only etch a few devices at the same time. the XeF_2 etching is isotropic process, so longer etching time should be avoided in order to gain an rectangular opening. Besides, I also noticed that after long time etching, it becomes

difficult to complete the wire boding. The reason for this is not clear. Another important pre-step before etching is dehydration of the system chuck. The XeF_2 would react with water and then etch the silicon nitride at a fast rate. What I did is heat the chuck at about 100°C for 3 minutes and let it cool to room temperature. After that, the etching process should be started immediately.

APPENDIX B

MICRO-CALORIMETER DETECTION LIMIT

To estimate the detection limit of the micro-calorimeter, we need to estimate the heat capacity of the calorimetry cell, in other words, the aluminum heater and silicon nitride membrane. The dimensions of effective heater part(the part sits on top of the membrane) and membrane and their properties [41, 42]are listed below:

So the heat capacities are

$$C_{Al} = 50 \times 10^{-9} \times 4 \times 10^{-3} \times 0.25 \times 10^{-3} \times 2700 \times 898.76 = 1.21 \times 10^{-7} J/K \tag{B.1a}$$

and

$$C_{SiN_x} = 100 \times 10^{-9} \times 4 \times 10^{-3} \times 3 \times 10^{-3} \times 3290 \times 400 = 1.579 \times 10^{-6} J/K \tag{B.1b}$$

The total heat capacity of the cell is $C_{cell} = C_{Al} + C_{SiN_x} \doteq 1.7 \times 10^{-6}$ J/K. From the DAQ 6259 manual, its sensitivity which is the smallest voltage change that can be detected is 112 μV in the $\pm 10V$ range. So the smallest temperature difference that can be detected is

$$\Delta T_{min} = \frac{\Delta V_{min}}{I} \frac{1}{dR/dT} = 0.2K \tag{B.2}$$

Table B.1: Dimensions and Properties of Calorimetric Cell

	Al	SiNx
Length	4 mm	4 mm
Width	0.25 mm	3 mm
Thickness	50 nm	100 nm
Density	2700 Kg/m^3	3290 Kg/m^3
Specific heat	898.76 J/Kg K	400J/Kg K

The energy balance for sample and reference sensors are Sample sensor

$$C_S = [C_R + C_{samp}] \cdot \frac{dT_s}{dt} = I_s \cdot V_s \tag{B.3a}$$

Reference sensor:

$$C_R \cdot \frac{dT_R}{dt} = I_R \cdot V_R \tag{B.3b}$$

During experiment, normally, $I_R = I_S = 28mA$ and $dt = 40 \times 10^{-6}s$, combine Equation B.3bandB.3a and apply those numbers, we can get

$$\begin{aligned} C_{samp} \cdot dT_s &= C_R \cdot (\underbrace{dT_R - dT_s}_{\Delta T_{min}}) - I \cdot dt \cdot (\underbrace{V_R - V_s}_{\Delta V_{min}}) \\ &\approx 3.4 \times 10^{-7} J \end{aligned} \tag{B.4}$$

APPENDIX C

ERROR ANALYSIS

There are multiple error sources in our experiment. Ref [27] explain the detailed procedure. Follow the analysis in Ref[27], to estimate the error, we can start from the basic equation of the calorimetry.

$$C_{samp} = \frac{V_s I_s}{dT_s/dt} - \frac{V_R I_R}{dT_R/dt} \tag{C.1}$$

The linear thermal expansion coefficient α is

$$\alpha = \frac{dR/dT}{R_0} \tag{C.2}$$

For the most common heater, $dR/dT = 0.02\Omega/K$ and the room temperature resistance $R_0 = 19\Omega$, so $alpha = 1.05 \times 10^{-3}$. The error of dT/dt can be expressed as

$$\varepsilon^2_{dT/dt} = \frac{2\varepsilon^2_{V_R}}{\alpha^2 V_R^2 (\Delta t)^2} + \frac{2\varepsilon^2_{V_{IR}}}{\alpha^2 V_{IR}^2 (\Delta t)^2} \tag{C.3}$$

where the subscript IR means the voltage on the external resistor which is used to measure I_{ref}.

According to [27], the dT/dt term is the main source, so the fractional error of C_p can be estimated by the fractional error of dT/dt ($\delta_{dT/dt} = \frac{\varepsilon_{dT/dt}}{dT/dt}$). We listed all the values needed to evaluate Equation C.3.

In Table C.1, we choose the current value used for most devices which is 28 mA, and we choose a typical value for the the resistance of the metal heater as 19Ω, the external resistor used for current measurement is 100Ω. The time step Δt here is the time interval between two measured point (in 10ms heating period, we have 250 data points). We can use the temperature rising rate as 40 K/ms. According to the DAQ 6259 manual, in our voltage range ($\pm 10V$),the gain error is 83 ppm and the offset error is 101 ppm,so the

Table C.1: Values Needed for Error Estimation

Parameter	Value
V_R	$28mA \times 19\Omega = 0.53V$
V_{IR}	$28mA \times 100\Omega = 2.8V$
α	$1.05 \times 10^{-3} K^{-1}$
ΔT	$40 \times 10^{-6} s$
Instrument error	184 ppm
Noise uncertainty	$83\mu V$

total error of the instrument is 184 ppm. Now we can calculate the absolute error ε_{V_R} and $\varepsilon_{V_{IR}}$ in EquationC.3.

$$\varepsilon_{V_R} = 0.53V \times 184 \times 10^{-6} + 83\mu V \doteq 83\mu V \tag{C.4a}$$

and

$$\varepsilon_{V_{IR}} = 2.8V \times 184 \times 10^{-6} + 83\mu V \doteq 598.2\mu V \tag{C.4b}$$

Apply those numbers, we can get the fractional error

$$\delta C_p \approx \delta(dT/dt) = \frac{\varepsilon_{dT/dt}}{dT/dt} = 0.229 \tag{C.5}$$

In calorimetry, we need to measure both the reference and sample device, hence fractional error of the measured sample heat capacity is expressed as

$$\delta C_{p,samp} \approx \frac{\sqrt{2} \cdot \delta C_p \cdot C_p}{C_{p,samp}} \times \frac{1}{\sqrt{n}} \tag{C.6}$$

where n stands for how many scans we used per calorimetry measurement, i.e. the number of pulses, typically, we can choose $n = 1200$. From previous appendix, we estimate $C_p \approx 1.7 \times 10^{-6} J/K$, for the heat capacity of polymer sample, we choose the value for the thickest one (60nm), which is $C_{p,samp} = 1 \times 10^{-7} J/K$, apply those numbers, the fractional error of the polymer sample heat capacity is about 15%.

Because our final result is specific error, the heat capacity is divided by the polymer sample volume. The polymer thickness is measured by ellipsometry, according to the instrument manual, the fractional error is about 3%, so the

total error of the specific heat capacity is

$$\begin{aligned}\delta &= \frac{\delta c_{p,samp}}{c_{p,samp}} \\ &= \sqrt{(\delta C_{p,samp})^2 + (\delta t)^2} \\ &= \sqrt{(15\%)^2 + (3\%)^2} = 15.3\% \end{aligned} \tag{C.7}$$

REFERENCES

[1] R. A. Huggins, Ed., *Thermal Energ Storage*. Springer, 2010, ch. 3, pp. 21–27.

[2] B. Zalba, J. M. Marín, L. F. Cabeza, and H. Mehling, "Review on thermal energy storage with phase change: materials, heat transfer analysis and applications," *Applied Thermal Engineering*, vol. 23, pp. 251–283, 2003.

[3] J. Wen, *Heat Capacities of Polymers*, 2nd ed. Springer, 2007, ch. 9.

[4] B. Chu, X. Zhou, K. Ren, B. Neese, M. Lin, Q. Wang, F. Bauer, and Q. M. Zhang, "A dielectric polymer with high electric energy density and fast discharge speed," *Science*, vol. 313, no. 5785, pp. 334–336, 2006.

[5] S. Fujieda, Y. Hasegawa, A. Fujita, and K. Fukamichi, "Thermal transport properties of magnetic refrigerants $La(Fe_xSi_{1-x})_{13}$ and their hydrides, and $Gd_5Si_2Ge_2$ and MnAs," *Journal of Applied Physics*, vol. 95, no. 5, pp. 2429–2431, 2004.

[6] H. Wada and Y. Tanabe, "Giant magnetocaloric effect of $MnAs_{1-x}Sb_x$," *Applied Physics Letters*, vol. 79, no. 20, p. 3302, 2001.

[7] I. Dincer, S. Dost, and X. Li, "Performance analyses of sensible heat storage systems for thermal applications," *International Journal of Energy Research*, vol. 21, no. 12, pp. 1157–1171, 1997.

[8] G. Faninger, *Sustainable solar housing: Strategies and solutions*. Earthscan Publication Ltd, 2007, ch. Sensible Heat Storage, p. 215.

[9] H. O. Paksoy, Ed., *Thermal Energy Storage for Sustainable Energy Consumption Fundamentals, Case Studies and Design*. Springer, 2007.

[10] M. A. Diner, brahim Rosen, *Thermal Energy Storage Systems and Application*. Wiley & Sons, Ltd, 2010, ch. Thermal Energy Storage (TES) Methods, pp. 83–190.

[11] P. H. M. Pierre Papon, Jacques Leblond, *The Physics of Phase Transition*. Springer, 2006.

[12] B. Sørensen, Ed., *Renewable Energy (Fourth Edition)*. Academic Press, 2011, ch. 5, pp. 533–605.

[13] H. P. N. L. N'Tsoukpoe, K. EdemLiu, "A review on long-term sorption solar energy storage," *Renewable and Sustainable Energy Reviews*, vol. 13, pp. 2385–2396, 2009.

[14] P. A. H. D. H. n. T. K. Bales, C.Gantenbein, "Thermal properties of materials for thermo-chemical storage of solar heat," Internaotional Energy Angency, Tech. Rep., 2005.

[15] Y. Kato, *Thermal Energy Storage for Sustainable Energy Consumption Fundamentals, Case Studies and Design*. Springer, 2007, ch. 23, pp. 393–408.

[16] P. J. D. K. H. S. K. V. E. M. W. R. Bales, C. Gantenbein, "Laboratory tests of chemical reactions and prototype sorption storage units report b4 of subtask b," International Energy Agency, Tech. Rep., 2008.

[17] J. van Berkel, "Solar thermal storage techniques," Entry Technology, Tech. Rep., 2000.

[18] J. Visscher, K. Veldhuis, "Comparison of candidate materials for seasonal storage of solar heat through dynamic simulation of building and renewable energy system," 2005.

[19] S. Krishnan and S. V. Garimella, "Thermal management of transient power spikes in electronicshase change energy storage or copper heat sinks?" *Journal of Electronic Packaging*, vol. 126, no. 3, pp. 308–316, 2004.

[20] F. L. Tan and C. P. Tso, "Cooling of mobile electronic devices using phase change materials," *Applied Thermal Engineering*, vol. 24, no. 2-3, pp. 159–169, 2004.

[21] A. Sharma, V. Tyagi, C. Chen, and D. Buddhi, "Review on thermal energy storage with phase change materials and applications," *Renewable and Sustainable Energy Reviews*, vol. 13, no. 2, pp. 318–345, 2009.

[22] M. M. Farid, A. M. Khudhair, S. A. K. Razack, and S. Al-Hallaj, "A review on phase change energy storage: materials and applications," *Energy Conversion and Management*, vol. 45, no. 9-10, pp. 1597–1615, 2004.

[23] S. A. Rinne, F. Garcia-Santamaria, and P. V. Braun, "Embedded cavities and waveguides in three-dimensional silicon photonic crystals," *Nat Photon*, vol. 2, no. 1, pp. 52–56, 2008, 10.1038/nphoton.2007.252.

[24] G. Guisbiers and L. Buchaillot, "Modeling the melting enthalpy of nanomaterials," *The Journal of Physical Chemistry C*, vol. 113, no. 9, pp. 3566–3568, 2009.

[25] Q. Mei and K. Lu, "Melting and superheating of crystalline solids: From bulk to nanocrystals," *Progress in Materials Science*, vol. 52, no. 8, pp. 1175–1262, 2007.

[26] D. W. Denlinger, E. N. Abarra, K. Allen, P. W. Rooney, M. T. Messer, S. K. Watson, and F. Hellman, "Thin film microcalorimeter for heat capacity measurements from 1.5 to 800 k," *Review of Scientific Instruments*, vol. 65, no. 4, pp. 946–959, 1994.

[27] M. Y. Efremov, E. A. Olson, M. Zhang, F. Schiettekatte, Z. Zhang, and L. H. Allen, "Ultrasensitive, fast, thin-film differential scanning calorimeter," *Review of Scientific Instruments*, vol. 75, no. 1, pp. 179–191, 2004.

[28] M. Efremov, "Thin-film differential scanning nanocalorimetry: heat capacity analysis," *Thermochimica Acta*, vol. 412, no. 1-2, pp. 13–23, 2004.

[29] D. W. Oxtoby, "New perspectives on freezing and melting," *Nature*, vol. 347, pp. 725–730, 1990.

[30] B. Wunderlich, "One hundred years research on supercooling and superheating," *Thermochimica Acta*, vol. 461, no. 1-2, pp. 4 – 13, 2007, 9th Laehnwitzseminar 2006 Special Issue, 9th Laehnwithseminar on Calorimetry. [Online]. Available: http://www.sciencedirect.com/science/article/B6THV-4MDWY28-1/2/2811fc233ef732d80d532d2a47c87a22

[31] L. H. S. M. L. T. J. L. K. Zhang, L. Zhang, "Superheating and melting kinetics of confined thin films," *Acta Materialia*, vol. 54, no. 13, pp. 3553–3560, 2006.

[32] L. Z. Z. H. J. L. H. Z. M. L. S. K. Lu, "Superheating of confined pb thin films," *Physical Review Letters*, vol. 85, no. 7, pp. 1484–1487, 2000.

[33] S. B. S. Nanda, K. Sahu, "Liquid-drop model for the size-dependent melting of low-dimensional systems," *Physical Review A*, vol. 66, no. 1, 2002.

[34] S. K. Yaman Yener, *Heat Conduction.* Taylor & Francis, 2008, ch. 11, pp. 341–374.

[35] M. Ghossoub, J.-H. Lee, O. Baris, D. Cahill, and S. Sinha, "Percolation of thermal conductivity in amorphous fluorocarbons," *Physical Review B*, vol. 82, no. 19, 2010.

[36] T. Easwarakhanthan, D. Beyssen, L. Le Brizoual, and J. Bougdira, "Spectroellipsometric analysis of CHF_3 plasma-polymerized fluorocarbon films," *Journal of Vacuum Science & Technology A: Vacuum, Surfaces, and Films*, vol. 24, no. 4, pp. 1036–1043, 2006.

[37] C. Schick, "Glass transition under confinement-what can be learned from calorimetry," *European Physical Journal: Special Topics*, vol. 189, no. 1, pp. 3–36, 2010, export Date: 3 January 2011 Source: Scopus.

[38] Y. P. Koh, G. B. McKenna, and S. L. Simon, "Calorimetric glass transition temperature and absolute heat capacity of polystyrene ultrathin films," *Journal of Polymer Science Part B: Polymer Physics*, vol. 44, no. 24, pp. 3518–3527, 2006.

[39] M. Y. Efremov, E. A. Olson, M. Zhang, Z. Zhang, and L. H. Allen, "Glass transition in ultrathin polymer films: Calorimetric study," *Physical Review Letters*, vol. 91, no. 8, p. 085703, 2003, copyright (C) 2011 The American Physical Society Please report any problems to prola@aps.org PRL.

[40] M. Asheghi, "Thermal transport properties of silicon films," Ph.D. dissertation, Stanford University, 1999.

[41] D. R. L. W. M. Mickey Haynes, *CRC Handbook of Chemistry and Physics (Internet Version 2011)*. CRC Press/Taylor and Francis, Boca Raton, FL, 2011, ch. THERMAL AND PHYSICAL PROPERTIES OF PURE METALS.

[42] B. L. Zink and F. Hellman, "Specific heat and thermal conductivity of low-stress amorphous si-n membranes," *Solid State Communications*, vol. 129, no. 3, pp. 199–204, 2004.

[43] E. A. Olson, M. Yu, Efremov, M. Zhang, Z. Zhang, and L. H. Allen, "The design and operation of a MEMS differential scanning nanocalorimeter for high-speed heat capacity measurements of ultrathin films," *JOURNAL OF MICROELECTROMECHANICAL SYSTEMS*, vol. 12, no. 3, pp. 355–364, 2003.

[44] C. Kittel and H. Kroemer, *Thermal physics*. WH Freeman & Co, 1980.

[45] J. R. E. Barker, "Grüneisen numbers for polymeric solids," *Journal of Applied Physics*, vol. 38, no. 11, pp. 4234–4242, 1967.

[46] J. G. Curro, "Calculation of Grüneisen parameters of polymers," *The Journal of Chemical Physics*, vol. 58, no. 1, pp. 374–380, 1973.

[47] Y. Wada, A. Itani, T. Nishi, and S. Nagai, "Grüneisen constant and thermal properties of crystalline and glassy polymers," *Journal of Polymer Science Part A-2: Polymer Physics*, vol. 7, no. 1, pp. 201–208, 1969.

[48] R. W. Warfield, "The Grüneisen constant of polymers," *Die Makromolekulare Chemie*, vol. 175, no. 11, pp. 3285–3297, 1974.

[49] D. O'Hagan, "Understanding organofluorine chemistry. an introduction to the CF bond," *Chem. Soc. Rev.*, 2007.

[50] G. K. White, "Thermal expansion of vitreous silica at low temperatures," *Physical Review Letters*, vol. 34, no. 4, p. 204, 1975, copyright (C) 2011 The American Physical Society Please report any problems to prola@aps.org PRL.

[51] G. J. Morgan, G. K. White, and J. G. Collins, "Thermal expansion of amorphous As_2S_3 at low temperatures," *Philosophical Magazine B: Physics of Condensed Matter; Electronic, Optical and Magnetic Properties*, vol. 43, no. 6, pp. 1039–1048, 1981, cited By (since 1996): 2 Export Date: 2 March 2011 Source: Scopus.

[52] G. K. White, S. J. Collocott, and J. S. Cook, "Thermal expansion and heat capacity of vitreous B_2O_3," *Physical Review B*, vol. 29, no. 8, p. 4778, 1984, copyright (C) 2011 The American Physical Society Please report any problems to prola@aps.org PRB.

[53] G. A. Saunders, R. D. Metcalfe, M. Cutroni, M. Federico, and A. Piccolo, "Elastic and anelastic properties, vibrational anharmonicity, and fractal bond connectivity of superionic glasses," *Physical Review B*, vol. 53, no. 9, p. 5287, 1996, copyright (C) 2011 The American Physical Society Please report any problems to prola@aps.org PRB.

[54] J. Fabian and P. B. Allen, "Thermal expansion and Grüneisen parameters of amorphous silicon: A realistic model calculation," *Physical Review Letters*, vol. 79, no. 10, p. 1885, 1997, copyright (C) 2011 The American Physical Society Please report any problems to prola@aps.org PRL.